 doi:10.20944/preprints202009.0664.v1

Article

The Optimum Method for Urban Land Surface Temperature Estimation

Ekkaluk Salakkham [1,2] and Pantip Piyatadsananon [1,*]

[1] School of Geoinformatics, Institute of Science, Suranaree University of Technology, Nakhon Ratchasima 30000, Thailand; pantip.p@sut.ac.th
[2] Department of Geography and Geoinformation, Faculty of Science, Buriram Rajabhat University Buriram 31000, Thailand; aekkarak.sk@bru.ac.th
* Correspondence: pantip.p@sut.ac.th; Tel.: +66-9551-426-59

Abstract: Land Surface Temperature (LST) estimation has been studied for several purposes, while the optimal method of estimating the LST has not been criticized yet. This research explores the optimum method in Land Surface Temperature (LST) estimation using LANDSAT-8 imagery data. Four different LST retrieval approaches, the Radiative Transfer Equation-based method (RTE), the Improved Mono-Window method (IMW), the Generalized Single-Channel method (GSC), and the Split-Window algorithm (SW), were calculated to present the LSTs over Buriram Town Municipality, Thailand. The calculated LSTs from these four methods were compared with the ground-based temperature data, taken on the same date and time of the employed LANDSAT-8 images. For this reason, the optimum method of the LST calculation was justified by considering the lowest normalized root means square error (NRMSE) values. As a result, the SW algorithm presents an optimum method in LST estimation. Regarding the SW, this algorithm requires not only the atmospheric profiles during satellite acquisition but also the retrieval of several coefficients. Besides, the LST retrieval method based on the SW algorithm is sensitive to water vapor content and coefficients. Although the SW algorithm is an optimum method explored in this study, it is emphasized that the adjustable values of coefficient response to the atmospheric state may be recommended. With these conditions, the SW algorithm can generate the land-surface temperature over the mixed land-use and land cover on the LANDSAT-8 images.

Keywords: radiative transfer equation; improved mono-window; generalized single-channel; split-window; LANDSAT-8; urban land surface temperature

1. Introduction

Land Surface Temperature (LST) is one of the most critical variables for estimating radiation and energy budgets associated with the mainland surface processes on regional and global scales [1-3]. Also, it is crucial for a wide variety of land-atmosphere studies [4,5]. Knowledge of the distribution of LST can provide useful information about the surface physical properties and climate, which plays a role in a variety of fields including land-atmosphere energy budget [6,7], climate change [7-9], hydrological cycle [7,9,10], evapotranspiration [8,10], and urban climate [6,10,11].

Regarding the data from satellite remote sensing, the LST data provides denser spatial sampling intervals than taken LST data at ground sites [12]. This remote sensing data provide a direct and continuous way to observe land surface characteristics and provides spatially continuous surface temperature information over large scales. The LST retrieval methods from remote sensing data made significant progress in obtaining the LST data. Data from the LANDSAT series is one of the most widely used satellite images for retrieving the LST according to its free downloadable data from the USGS website, regular revisit times, and long-term recorded data. LANDSAT-8 was successfully

launched in 2013 and deployed into orbit with two instruments onboard, the Operational Land Imager (OLI) and the Thermal Infrared Sensor (TIRS) with two spectral bands in the Long Wavelength Infrared (LWIR) [15]. As the essential data, band 11 is significantly more contaminated by stray light than Band 10. It is recommended that users refrain from using Band 11 data in the quantitative analysis, including Band 11 in split-wind surface temperature retrieval algorithms [16]. The LST estimation algorithms, with the Land Surface Emissivity (LSE), are known a priori, can be roughly grouped into three categories: multi-angle methods, multi-channel methods, and single-channel methods [17,18].

The LSE is a proportional factor that scales blackbody radiance (Planck's law) to predict emitted radiance. It is also the efficiency of transmitting thermal energy across the surface into the atmosphere [20]. Weng, *et al.* [21] indicated that the estimation of emissivity for ground objects from passive sensor data could be measured using different techniques. For instance, the Normalized Difference Vegetation Index (NDVI) was used as a threshold to designate emissivity values [22]. Regarding this method, it considers the internal reflections (cavity effects) caused by a heterogeneous surface. Accordingly, validation studies for complex terrains are more complicated [23]. Liu, *et al.* [24] and Coll *et al.* [25] noted that a previous study [26] performed over the large, fully vegetated surface and bare surfaces or deserts, where relatively homogeneous test sites to avoid uncertainty due to spatial heterogeneity. The land surface is generally heterogeneous at the satellite pixel-level; furthermore, promising temperature-based validation is based upon in-situ measurements limits to homogeneous land surface types. Therefore, the accuracy of LSTs retrieved from heterogeneous or mixed pixels remains questionable.

This research explores the optimum method in LST estimation over the different land covers by using LANDSAT-8 imagery data. For this reason, four different LST retrieval approaches, RTE, IMW, GSC, and SW, are calculated to present the LSTs over Buriram Town Municipality, Thailand. Eventually, the calculated LSTs were compared with the ground-based temperature data from the surveying on the same date and time of the obtained LANDSAT-8 data. The optimum method of the LST calculation is concluded and discussed regarding the lowest normalized root means square error (NRMSE) values.

2. Materials and Methods

2.1 Study Area

Buriram province locates in the North-Eastern region of Thailand. Buriram province has been overgrowing in the last decade, especially in the Town Municipality. Buriram Town Municipality covers 6,000,000 sq. meters (or six sq. kilometers) with heterogeneous land cover characteristics (Figure 1). Over 30,000 residences are living in the municipality [27]. Moreover, it has encountered rapid urbanization due to the mega-sport complex. The mega-sports complex contains a massive stadium for the football field and races motor tracks [28]. This mega-sports complex attracts many tourists and drives the built-up constructions over Buriram Town Municipality developed by the provincial governor [29].

 doi:10.20944/preprints202009.0664.v1

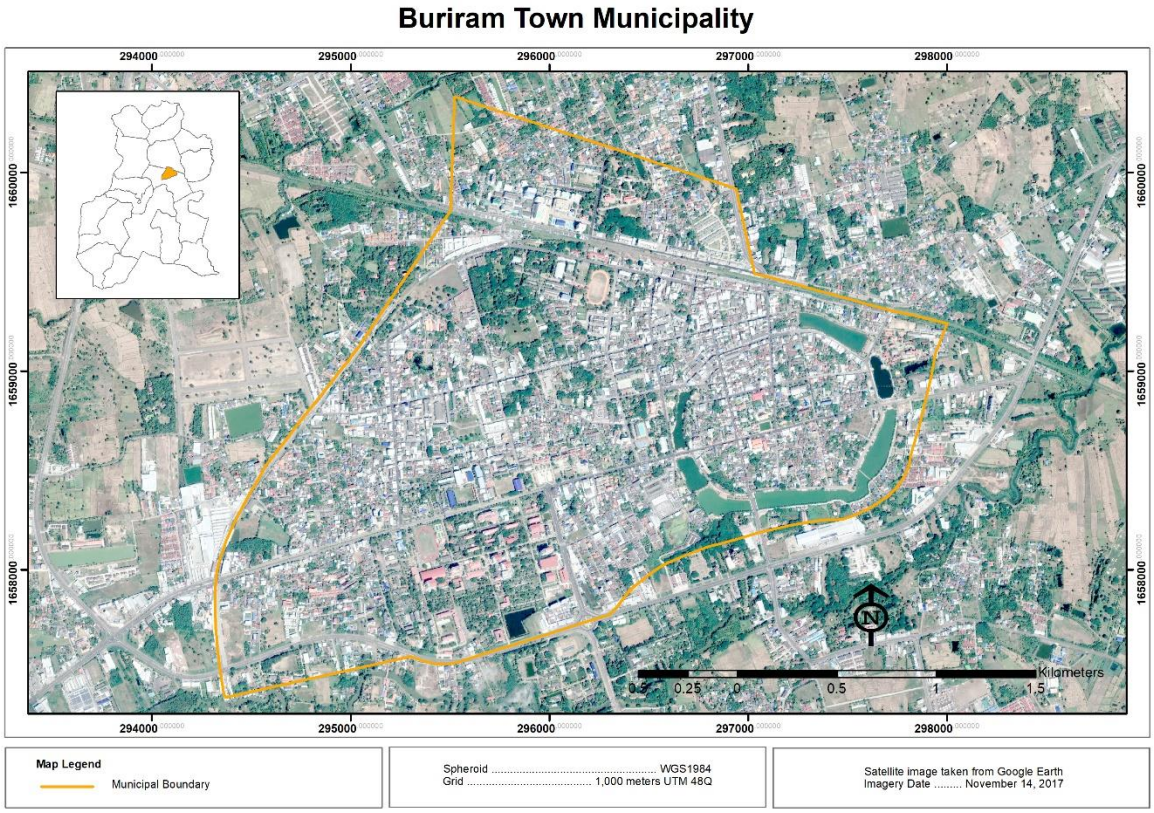

Figure 1. Buriram Town Municipality.

2.2 Datasets

This study used the data extracted from LANDSAT-8 imagery, path 128 - row 50, obtained on January 21st, February 6th, March 26th, and April 11th in 2018. They were used for the LST estimation. It means that the study area was investigated monthly from January to April 2018. Within these four months, land-use and land-cover had not yet been changed. Therefore, very high-resolution imagery (5 cm. GSD: Ground Sampling Distance) captured from UAV (Unmanned Aerial Vehicle) in March 2018 was used for accuracy assessment. The data surveyed by the UAV shows the ground-based temperature over the study area.

2.3 Method

A conceptual framework of this study is illustrated in Figure 2. The method consists of three parts, (1) ground-based temperature measurement, (2) LST estimation, and (3) the comparison between ground-based temperature data and the estimated LST data to investigate the optimum method in LST estimation by considering the lowest NRMSE values.

Preprints (www.preprints.org) | NOT PEER-REVIEWED | Posted: 27 September 2020 doi:10.20944/preprints202009.0664.v1

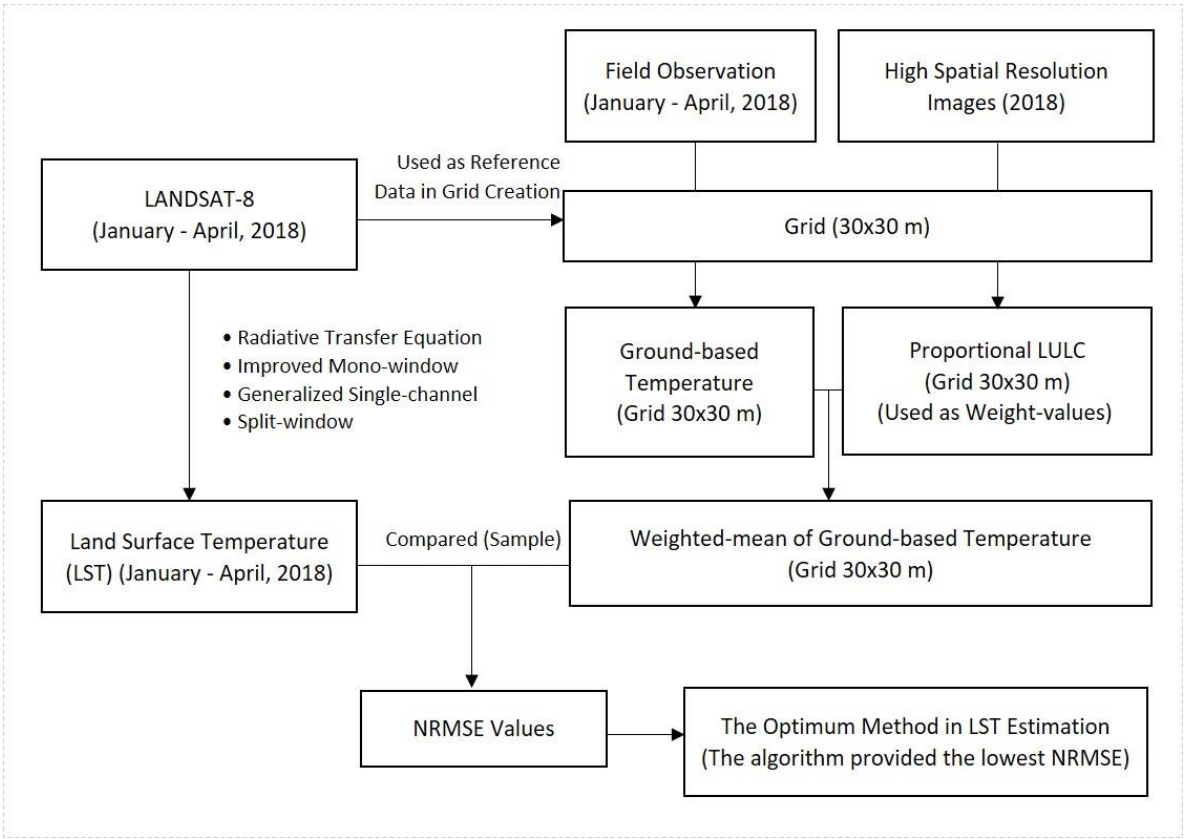

Figure 2. Conceptual Framework

2.3.1 Ground-based temperature measurement

The LANDSAT-8 image contains 30x30 meter-grids, whereas the thermal band image consists of 100x100 meter-grids. Therefore, an aggregated pixel as 3x3 pixels (90x90 m.) was assigned regarding the resemblance of the Thermal image's pixel size (100x100 m.). Based on the 3x3 pixels, the coverage area of pixel size is 8,100 sq. meters. The total study area is about six million sq. meters. As a result, the total number of sample points is 900 points.

Regarding the 3x3 pixels in which nine neighboring points were collected, respond to a single pixel of the thermal band. At least 83 sites are theoretically investigated; therefore, the ground-surface temperature of 100 sites was obtained using the stratified random method, shown in Figure 3.

(a) (b)

Figure 3. (a) Sample sites over the LANDSAT-8 imagery data; (b) high-resolution image from UAV

Preprints (www.preprints.org) | NOT PEER-REVIEWED | Posted: 27 September 2020 doi:10.20944/preprints202009.0664.v1

Based on Figure 3 (a), red grids are sample points response to the LANDSAT-8 imagery data, and orange girds are the locations of the site. One-hundred ground-based data of a very-high-resolution image from UAV was collected from nine neighboring sample points within a location site shown as an orange grid, as shown in Figure 3 (b). This process shows the accuracy assessment between the generated temperature from the LANDSAT-8 data and the ground-based temperature on the UAV image. The distribution of sample points and sample sites are shown in Figure 4.

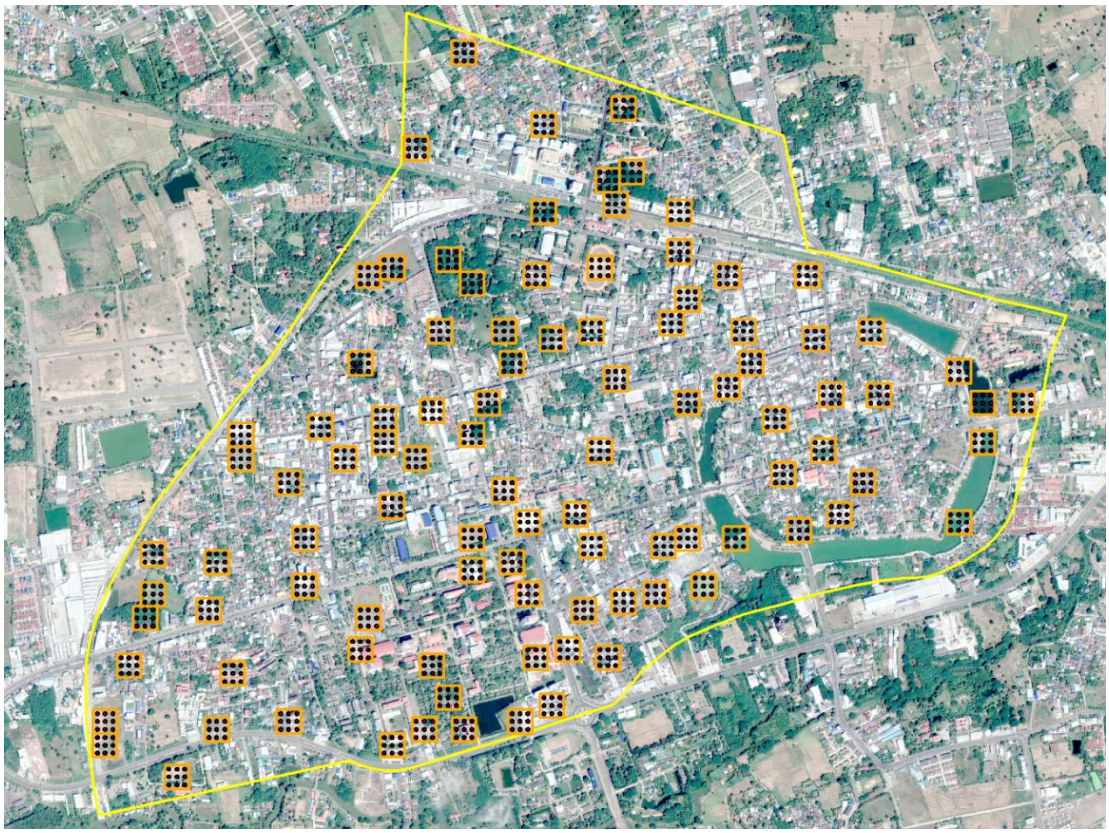

Figure 4. Distribution of sample points and sample sites.

The numbers of sample sites are 100 points. One sample site contains nine sample points; therefore, the total sample points are 900 points. All samples were collected within the yellow boundary of the Buriram municipality.

Ground-based temperature data were collected on the same date as the retrieved data from the LANDSAT-8 image. The temperature within each grid was measured and averaged using the weighted mean method regarding the land use and land cover (LULC). The weighted value was calculated from the areas of each LULC type, which was extracted from high spatial resolution image data from the UAV. Then the weighted-average temperature from each grid was used as the reference data and compared with the estimated Urban Land Surface Temperature (ULST data). These processes were applied to all four methods.

2.3.2 LST Estimation

In the second part, the ULST (Urban Land Surface Temperature) data were extracted using RTE, IMW developed by Wang, F. *et al.* [30], GSC developed by Jimenez-Munoz, J.C. et al. [31], and SW developed by Jimenez-Munoz, J.C. and others [31]. The relevant parameters were defined in a list after each equation.

Preprints (www.preprints.org) | NOT PEER-REVIEWED | Posted: 27 September 2020 doi:10.20944/preprints202009.0664.v1

1) Radiative transfer equation-based method (RTE)

For the RTE method, the atmospheric profile was extracted from the NCEP (National Centers for Environmental Prediction) dataset and used to simulate atmospheric transmittance, up-welling and down-welling radiance from the Moderate-resolution atmospheric Transmission (MODTRAN) model. Based on the radiative transfer equation, it is possible to estimate LST by Plank's law inversion [32], as the following expression.

$$LST = \frac{C_2}{\lambda \ln\left\{\frac{C_1}{\lambda^5\left[\frac{L_{sensor} - L_u - \tau(1-\varepsilon)L_d}{\tau\varepsilon}\right]} + 1\right\}} \quad (1)$$

Where L_{sensor} is thermal radiance at the sensor level, ε is land-surface emissivity, τ is atmospheric transmissivity, L_u and L_d are up-welling and down-welling atmospheric radiance, respectively, and C_1 and C_2 are the constant-coefficient.

2) Improved mono-window method

To avoid the dependence on radiosounding in the RTE method, Qin *et al.* [33] developed the Mono-Window algorithm for estimating the LST from LANDSAT-5 [34]. It was consequently developed as the Improved Mono-Window method for obtaining LST from LANDSAT-8 in 2015 [30], as the following expression.

$$LST = \frac{1}{C}[a(1-C-D)+(b(1-C-D)+C+D)T_B - DT_a] \quad (2)$$

$$With\ C = \varepsilon\tau$$

$$D = (1-\tau)[1+(1-\varepsilon)\tau]$$

Where a and b are constant coefficients, ε is the land surface emissivity, τ is the total atmospheric transmissivity, T_B is the at-sensor brightness temperature, and T_a is the mean atmospheric temperature.

3) Generalized single-channel method

In 2003, Jimenez-Munoz and Sobrino [35] developed the Generalize Single-Channel algorithm to estimate the LST from LANDSAT-5. It was developed to be the generalized single-channel method in 2014 by [31] for obtaining LST from LANDSAT-8 as the following expression.

$$LST = \gamma[\varepsilon^{-1}(\psi_1 L_{sensor} + \psi_2) + \psi_3] + \delta \quad (3)$$

$$With\ \gamma = \frac{T_B^2}{b_\gamma L_{sensor}} \quad (4)$$

$$\delta = T_B - \frac{T_B^2}{b_\gamma} \quad (5)$$

Where L_{sensor} is thermal radiance at the sensor level, b_γ equal 1,324 K, and 1,199 K for TIRS-1 (Band 10) and TIRS-2 (Band 11), respectively, T_B is at-sensor brightness temperature, ε is the land surface emissivity, and ψ_1, ψ_2, ψ_3 can be obtained as a function of the total atmospheric water vapor content (w).

4) Split-window algorithm

The Split-Window algorithm was developed by Jimenez-Munoz *et al.* Jimenez-Munoz, Sobrino, Skokovic, Matter and Cristobal [31],[32] as the following expression.

Preprints (www.preprints.org) | NOT PEER-REVIEWED | Posted: 27 September 2020 doi:10.20944/preprints202009.0664.v1

$$T_s = T_i + C_1(T_i - T_j) + C_2(T_i - T_j)^2 + C_0 + (C_3 + C_4 w)(1 - \varepsilon) + (C_5 + C_6 w)\Delta\varepsilon \quad (6)$$

Where C_0 to C_6 is the Split Window coefficients, T_i and T_j are at-sensor brightness temperature of the band i and j, respectively, ε is the land surface emissivity which obtained from $\varepsilon = 0.5(\varepsilon_i + \varepsilon_j)$ and $\Delta\varepsilon = (\varepsilon_i - \varepsilon_j)$.

2.3.3 Atmospheric parameters

The atmospheric parameters used in the LST estimation in each method are listed in Table 1.

Table 1. Parameters used in the LST estimation.

		Jan 21st	Feb 6th	Mar 26th	April 11th
Temperature (T_0) (K)		303.9	293.1	302.9	309.3
Relative Humidity		0.63	0.60	0.65	0.44
Water Vapor Content		2.86	1.52	2.79	2.72
Methods	**Atmospheric Parameters**	**Jan 21st**	**Feb 6th**	**Mar 26th**	**Apr 11th**
RTE	Transmittance (τ) [1]	0.53	0.80	0.54	0.60
	Up-welling	3.92	1.63	3.78	3.56
	Down-welling	6.00	2.67	5.86	5.65
IMW	Atmospheric Temperature (T_a)(K)	296.69	286.79	295.78	301.65
	Transmittance (τ) [2]	0.65	0.80	0.65	0.65
GSC	Atmospheric Function (ψ_1)	1.42	1.15	1.41	1.39
	Atmospheric Function (ψ_2)	-7.25	-2.97	-6.99	-6.70
	Atmospheric Function (ψ_3)	3.69	1.81	3.60	3.49
SW	Water Vapor Content	2.86	1.52	2.79	2.72

Note: 1 Transmittance, up-welling, and down-welling used in the RTE method were obtained from NCEP
2 The transmittance used in IMW was calculated based on the Mono-window method.

The near-surface air temperature (T_0) and relative humidity were received from Huai Rat Station near Buriram Town Municipality. These data have been updated on the Hydro and Agro Informatics Institute (HAII) website. Regarding a study of these parameters, they were used in the water vapor content calculation and estimated using the following expression [36].

$$w_i = \left\{0.59 \times RH \times \exp\left[\frac{17.27 \times (T_0 - 273.15)}{237.3 + (T_0 - 273.15)}\right]\right\} + 0.1697 \quad (7)$$

Where w_i is the water vapor content (g cm^{-2}), T_0 is the near-surface air temperature (K), and RH is the relative humidity (Decimal). The water vapor content, near-surface air temperature, and relative humidity are the average values.

The water vapor content has been used in the transmittance calculation in the IMW algorithm, the atmospheric function, the GSC algorithm, and the SW algorithm. The water vapor content calculation is also used in the atmospheric temperature (T_a) calculation, an essential parameter in the IMW algorithm.

The employed parameters are criticized in several points to propose the strengths and weaknesses of the model implementation. Firstly, the transmittance, up-welling, and down-welling atmospheric radiance are obtained from the NASA atmospheric correction parameter calculator. The calculator uses the National Centers for Environmental Prediction (NCEP) to model global

Preprints (www.preprints.org) | NOT PEER-REVIEWED | Posted: 27 September 2020 doi:10.20944/preprints202009.0664.v1

atmospheric profiles which are interpolated to a particular date, time, and location as input for the MODTRAN radiative transfer code and as a suite of the integrative algorithm to infer the up-welling, down-welling radiances and site-specific transmission [6]. The profiles resulting from time interpolation provide the closet lat/long position or specific location [19]. Lastly, calculating the atmospheric parameters in the Tropical region, the Mid-Latitude Simmer Model is usually employed due to the lack of atmospheric parameters in the Tropical Model.

2.3.4 Land Surface Emissivity

Another crucial parameter in LST estimation is Land Surface Emissivity, a variable with wavelength. Then the NDVI threshold method can be used to estimate the emissivity of different land surfaces in the 10-12 μm range. As mentioned by a study of Wang *et al.* [30] stated that the spectral range of Band 10 of LANDSAT-8 is suitable in this range. The emissivity of the pixel was determined based on the NDVI. The land surface emissivity can be calculated from the following expression [34].

$$\varepsilon = mP_v + n \quad (8)$$

$$\text{With} \quad m = \varepsilon_v - \varepsilon_s - (1-\varepsilon_s)F\varepsilon_v \quad (9)$$

$$n = \varepsilon_s + (1-\varepsilon_s)F\varepsilon_v \quad (10)$$

Where F is a shape factor whose mean value, assuming the different geometrical distribution is 0.55, ε_s and ε_v are emissivity of soil and vegetation, respectively.

2.3.5 The comparison between ground-based temperature data and the estimated LST data

As the final part, weighted-average temperature values calculated from the received data of each grid were compared with estimated ULST data. The NRMSE facilitates the comparison between datasets or models with different scales. The small value of NRMSE presents an optimum method of LST estimation.

$$\text{NRMSE} = \frac{\text{RMSE}}{\text{maximum observation - minimum observation}} \quad (11)$$

Where RMSE is Root Mean Square Error, which can be calculated as followed.

$$\text{RMSE} = \sqrt{\frac{1}{n}\sum(\text{estimate value - observe value})^2} \quad (12)$$

Where Estimate and Observe are the ground-based temperature data and the estimated LST data.

3. Results

The estimated LST data on January 21st, February 6th, March 26th, and April 11th in 2018 are illustrated in Figure 5 - 8, respectively. Furthermore, the average, maximum, and minimum LST data are shown in Table 2, the NRMSE result is shown in Table 3 and Figure 9 - 10.

Preprints (www.preprints.org) | NOT PEER-REVIEWED | Posted: 27 September 2020 doi:10.20944/preprints202009.0664.v1

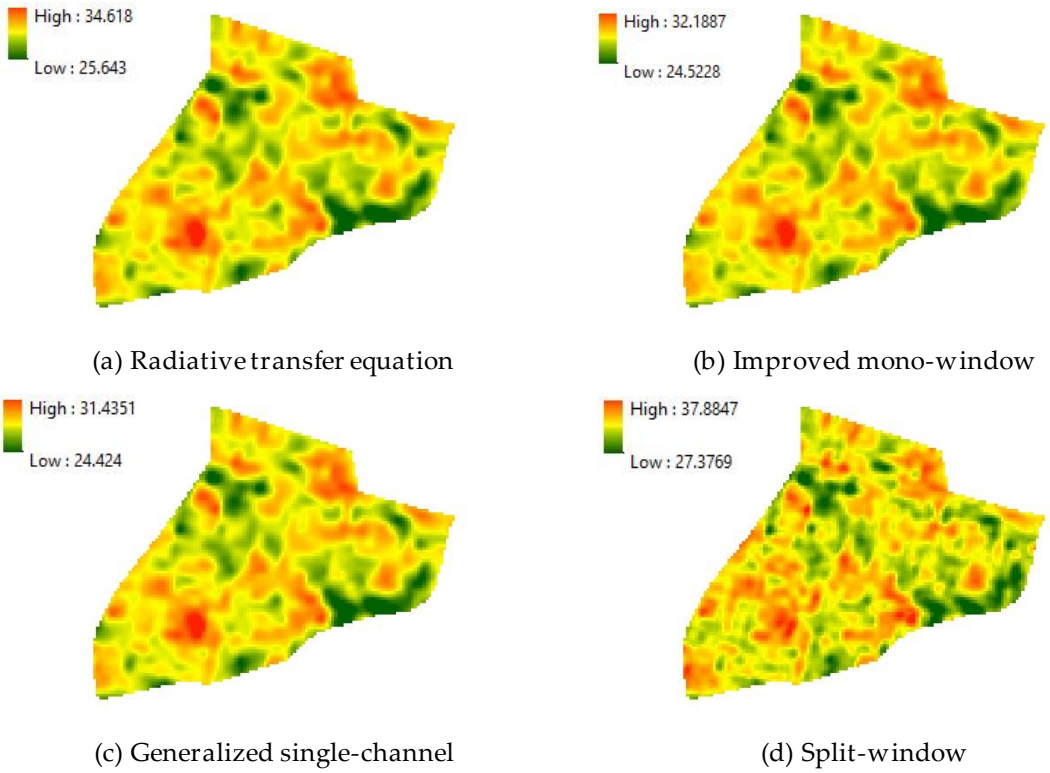

(a) Radiative transfer equation (b) Improved mono-window

(c) Generalized single-channel (d) Split-window

Figure 5. Estimated LST data on January 21st, 2018 from different technics

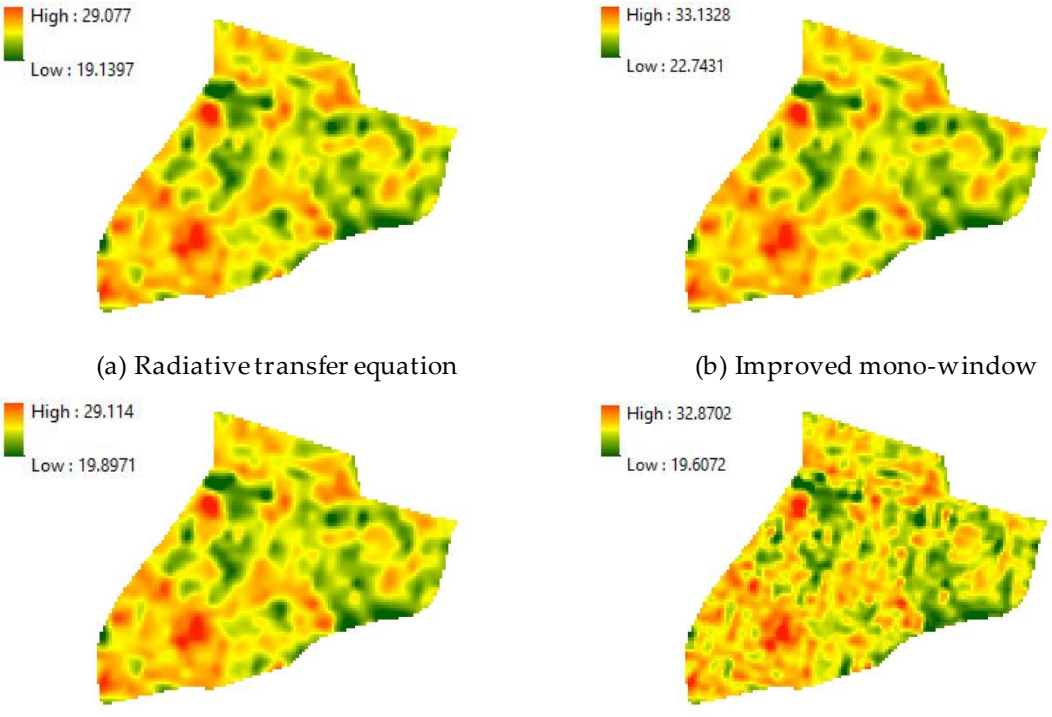

(a) Radiative transfer equation (b) Improved mono-window

(c) Generalized single-channel (d) Split-window

Figure 6. Estimated LST data on February 6th, 2018 from different technics

Preprints (www.preprints.org) | NOT PEER-REVIEWED | Posted: 27 September 2020 doi:10.20944/preprints202009.0664.v1

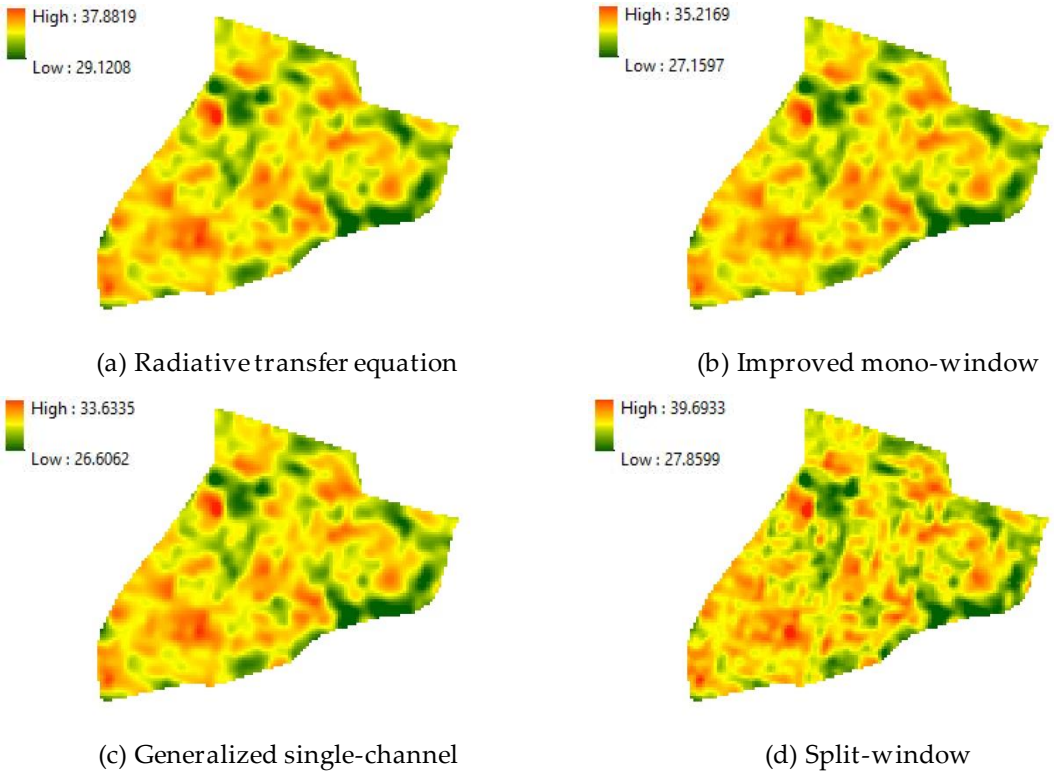

(a) Radiative transfer equation (b) Improved mono-window

(c) Generalized single-channel (d) Split-window

220 **Figure 7.** Estimated LST data on March 26th, 2018 from different technics

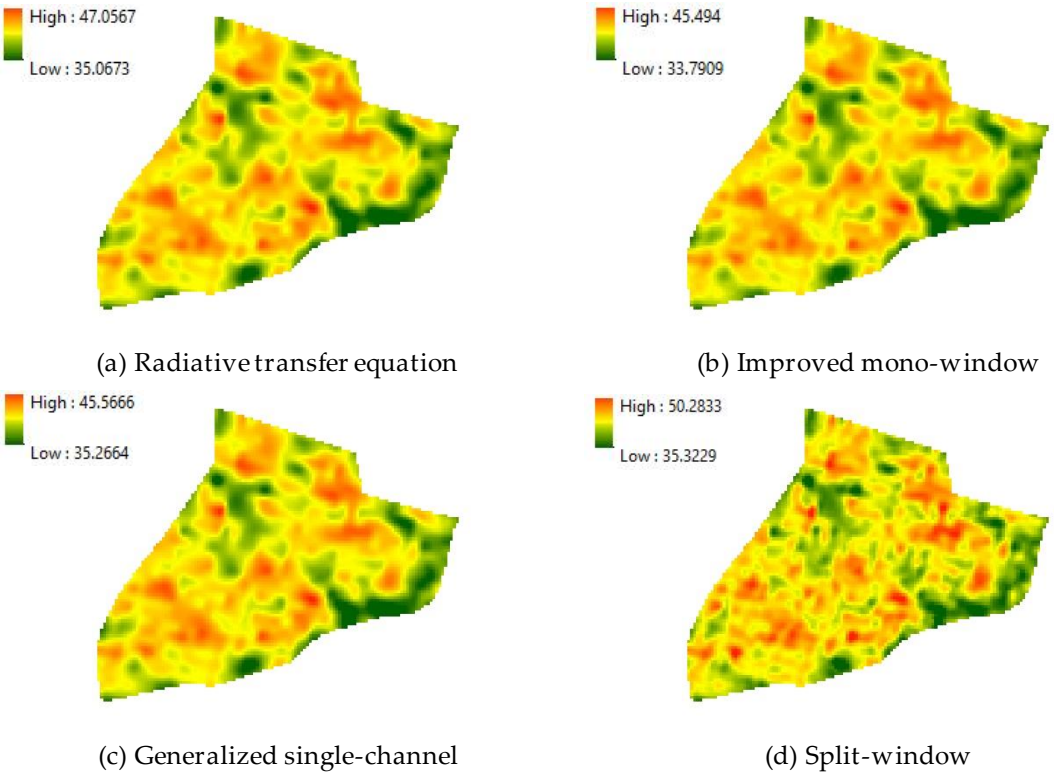

(a) Radiative transfer equation (b) Improved mono-window

(c) Generalized single-channel (d) Split-window

221 **Figure 8.** Estimated LST data on April 11th, 2018 from different technics

222 Based on Figure 5 - 8, the cold spots always occur in the North-West and South-East area of the
223 city, which are urban forest areas. This LULC type presents a lower temperature than other LULC

Preprints (www.preprints.org) | NOT PEER-REVIEWED | Posted: 27 September 2020 doi:10.20944/preprints202009.0664.v1

types. In contrast, high temperature always occurs in the bare-land and built-up area. Furthermore, the explored results from the single-channel methods, namely, RTE, IMW, and GSC, are almost the same, while the examined results from SW is different since the SW results are more complex surface than others.

Table 2. Average, maximum, and minimum LST data (°C)

		January 21st, 2018	February 6th, 2018	March 26th, 2018	April 11th, 2018
RTE	Average	30.821	25.258	34.087	42.330
	Maximum	34.618	29.077	37.882	47.057
	Minimum	25.643	19.140	29.121	35.067
IMW	Average	28.863	29.242	31.785	40.883
	Maximum	32.189	33.134	35.217	45.494
	Minimum	24.523	22.744	27.160	33.791
GSC	Average	28.444	25.573	30.590	41.494
	Maximum	31.435	29.114	33.633	45.567
	Minimum	24.424	19.897	26.606	35.266
SW	Average	33.863	27.640	34.602	43.465
	Maximum	37.885	32.872	39.693	50.283
	Minimum	27.377	19.608	27.860	35.323

Based on Table 2, the SW result shows the highest average LST data as 33.863 °C in January, followed by the RTE result and the IMW result: 30.821 °C and 28.863 °C, respectively. As the next month, the IMW result shows the highest average LST data as 29.242 °C, followed by the SW result and the GSC result as 27.640 °C and 25.573 °C, respectively, in February. In March, the SW result shows the highest average LST data as 34.602 °C, followed by the RTE result and the IMW result as 34.087 °C and 31.785 °C, respectively. Lastly, the SW also shows the highest average LST data as 43.465 °C, followed by the RTE and the GSC result as 42.330 °C and 41.494 °C, respectively, in April.

The highest average LST data occurs in April, followed by March and January, respectively. The LST data were the lowest due to the drop-down temperature in February. The most of SW results showed the highest average LST data as 33.863 °C, 34.602 °C, and 43.465 °C in January, March, and April, respectively. The IMW result showed the most upper average LST data as 29.242 °C. In contrast, the GSC results showed the lowest average LST data as 28.444 °C and 30.590 °C in January and March, respectively. The RTE result showed the lowest average LST data in February, and the IMW result showed the lowest LST average data in April.

Table 3. NRMSE Values

Date	NRMSE			
	RTE	IMW	GSC	SW
January 21, 2018	0.454	0.613	0.650	0.227
February 6, 2018	0.702	0.317	0.671	0.473
March 26, 2018	0.246	0.416	0.509	0.218
April 11, 2018	0.165	0.226	0.202	0.132
Overall NRMSE	0.171	0.181	0.219	0.114

Preprints (www.preprints.org) | NOT PEER-REVIEWED | Posted: 27 September 2020 doi:10.20944/preprints202009.0664.v1

Considering Table 3, the SW provides the lowest NRMSE values as 0.227 in January, followed by the RTE result, and the IMW result as 0.454 and 0.613, respectively. In February, the IMW result shows the lowest NRMSE value of 0.317, followed by the SW and the GSC as 0.473 and 0.671. In March, the SW result shows the lowest NRMSE values like 0.218, followed by the RTE result and the IMW result as 0.246 and 0.416, respectively. Lastly, in April, the SW result shows the lowest NRMSE value of 0.132, followed by the RTE and GSC as 0.165 and 0.202. Considering the overall NRMSE, the SW provides the lowest NRMSE values (0.114), followed by the RTE, IMW, and GSC, 0.171, 0.181, and 0.219.

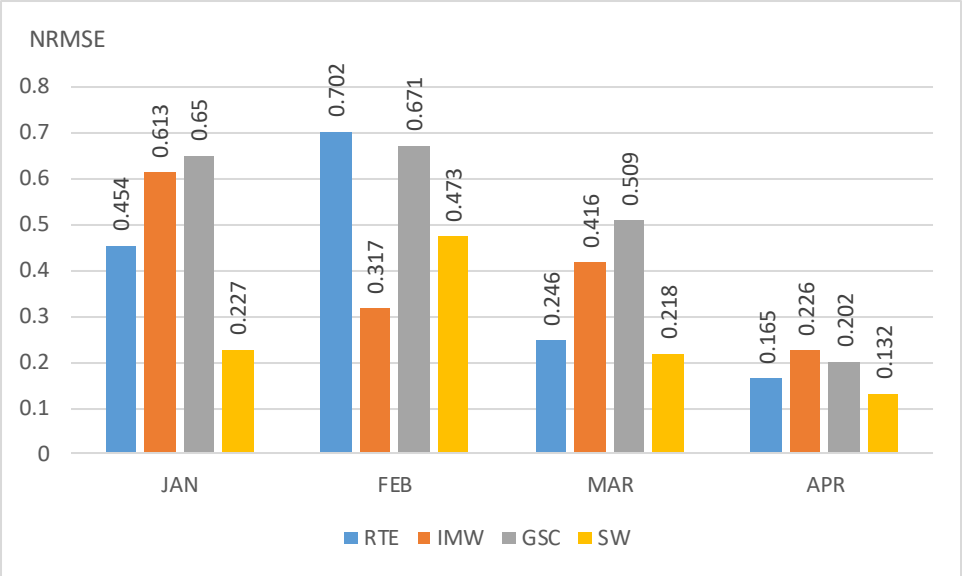

Figure 9. NRMSE values based on monthly results

Based on Figure 9, the SW algorithm provides the lowest error in January, as 0.227, followed by the RTE algorithm (0.454) and the IMW algorithm (0.613). In February, the IMW algorithm provides the lowest error as 0.317, followed by the SW algorithm (0.473) and the GSC algorithm (0.671). The results in March are similar to January, in which the SW algorithm provides the lowest error as 0.218, followed by the RTE algorithm (0.246) and the IMW algorithm (0.416), respectively. In April, the SW algorithm also presents the lowest error as 0.132, followed by the RTE algorithm (0.165) and the GSC algorithm (0.202).

Preprints (www.preprints.org) | NOT PEER-REVIEWED | Posted: 27 September 2020 doi:10.20944/preprints202009.0664.v1

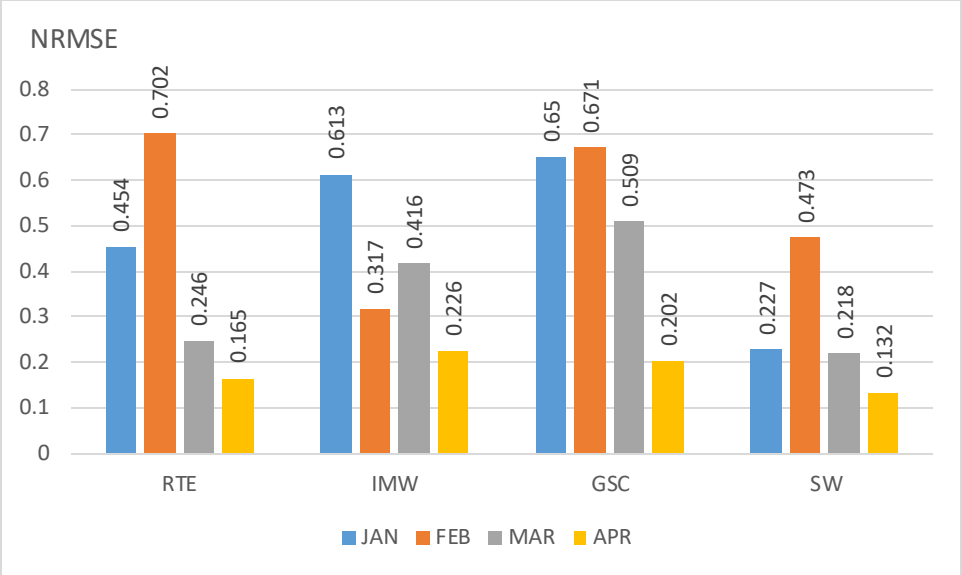

Figure 10. NRMSE values regarding LST estimation methods.

Based on Figure 10, most of all algorithms (RTE, GSC, and SW) present the highest NRMSE in Feb, but the IMW algorithm. In contrast, the SW algorithm remarkably performs the optimum method in estimating the LST in the typical dry period (December to April annually).

4. Discussion

As addressed in a study by Jimenez-Munoz, *et al.* [38] whether all of the single-channel methods, RTE, IMW, and GSC, apply only one thermal channel in LST estimation and require an accurate value of atmospheric parameters such as transmissivity, atmospheric up-welling, and down-welling radiance, atmospheric water vapor content, and air temperature. Besides, Coll, *et al.* [39] found that the accuracy of the single-channel method depends on the efficiency of the RTM and the atmospheric profiles representing the real state of the atmosphere over the study area at the time of the satellite measurements. Focusing on the RTE results, the error in this study may come from the atmospheric model used to calculate the atmospheric parameters. The study area locates in the tropical zone, while the atmospheric model provided by the NCEP model offers only the mid-latitude summer and mid-latitude winter models. On the other hand, the atmospheric parameters used in the IMW algorithm, the GSC algorithm, and the SW algorithm are directly based on the water vapor content values. This parameter was estimated based on the near-surface air temperature (T_0) and relative humidity values taken from the local meteorological station. It confirms that any large area, which few relative humidity values provided by the local meteorological station, may present significant errors in LST estimation.

Based on the IMW results, the error also comes from the near-ground air temperature (T_0) used in the sufficient atmospheric temperature (T_a) estimation. Another weak point is the lack of the obtained air temperature in the calculation [40]. The relationship between transmittance and water vapor content depends on not well-defined "high" and "low" air temperature values, whereas the relationship between T_a and T_0 are given for absolute standard atmospheres [38].

Based on the GSC results, this algorithm provides a higher error than other methods. The basis of this algorithm, criticized in a study by Jimenez-Munoz *et al.* [38], relies on estimating the so-called atmospheric function, which is always dependent only on water vapor content values. It was

recommended by Chen *et al.* [41] and Cristobal *et al.* [40] whether these atmospheric functions may be obtained more precisely from water vapor content and air temperature but through more complex models. Since input data are minimized to only one atmospheric parameter, an error in water vapor content estimation could increase the error in the LST retrievability of the single-channel algorithm. Furthermore, the possible errors in LST retrieval of the GSC algorithm are also expected to increase with atmospheric water vapor content [30,35].

Based on the SW results, this algorithm provides the lowest NRMSE. The accurate information about the atmospheric profiles during satellite acquisition seems not a significant issue [42]. In contrast, this algorithm requires the retrieval of several coefficients. Therefore, it can be concluded that the LST retrieval method is sensitive to water vapor content estimated error and also the coefficients. In this study, the coefficients were based on the study by Jimenez-Munoz *et al.* [31]. The coefficients depend on the atmospheric state, but sometimes fixed values are utilized, imposing significant errors. Apart from the atmospheric correction parameters, the surface emissivity is also required [19]. However, these methods assume that the surface is homogeneous, and the radiances are directly correlated with the emissivity values of materials and derived to LST. However, these emissivity values are generally based on land cover classification data, which have not considered the multiple scattering and reflection caused by urban geometry [44]. The study area, Buriram Town Municipality, is a more complicated phenomenon and heterogeneous spectral.

The multi-angles method is similar to the principle of the split-window algorithm yet different absorption due to varying atmospheric path-lengths from different observational angles. A significant benefit of these technics is that the measurements can be made from one satellite or simultaneously from two satellites [45]. Furthermore, the Multi-channels method or the split window requires two spectral bands at approximately 11 and 12 μm, which are affected by different atmospheric absorption. It assumes that the emissivity data in the multi-channels are similar [46]. Land surface brightness temperatures are then calculated as a linear combination of the two channels [47]. The algorithm does not require an atmospheric profile, while an integrated water vapor content is essential in the calculation [48]. However, a significant disadvantage of this approach is the coefficients, which are only valid for the ad hoc datasets [46].

5. Conclusions

Most of all algorithms (RTE, GSC, and SW) present the highest NRMSE in Feb, but the IMW algorithm. To answer this situation clearly, it was noticeable that the land surface of the study area contained much moisture due to the rain. The water vapor content is used in the transmittance calculation in the IMW algorithm. The water vapor content calculation is also used in the atmospheric temperature (T_a) calculation, an essential parameter in the IMW algorithm. Therefore, the IMW algorithm would provide the closest result to the humid day. It is considered as an extraordinary phenomenon for the raining days in February. This unexpected event may affect the LST calculations of those algorithms, but IMW. Considering the lowest NRMSE, it presents the SW algorithm as an optimum method in USLT estimation for this study. The errors may occur due to the atmospheric parameter estimation and emissivity estimation, while the amount of atmospheric water vapor content data plays a significant role in the calculation. It is noted that the atmospheric water vapor content data must be carefully considered regarding the use of the SW algorithm. Furthermore, regarding these explored results, it can be concluded that the amount of atmospheric water vapor content plays an essential role in accuracy assessment.

Author Contributions: Conceptualization, Ekkaluk Salakkham and Pantip Piyatadsananon; methodology, Ekkaluk Salakkham and Pantip Piyatadsananon; software, Ekkaluk Salakkham; validation, Ekkaluk Salakkham

and Pantip Piyatadsananon; formal analysis, Ekkaluk Salakkham; investigation, Ekkaluk Salakkham; data curation, Ekkaluk Salakkham; writing-original draft preparation, Ekkaluk Salakkham; writing-review and editing, Pantip Piyatadsananon; supervision, Pantip Piyatadsananon All authors have read and agreed to the published version of the manuscript.

Funding: This research received no external funding.

Acknowledgments: One Research One Graduate scholarship of SUT granted to Ekkaluk Salakkham. The special thanks from the authors go to anonymous reviewers for their valuable comments and suggestions that improve our manuscript from various perspectives.

Conflicts of Interest: The authors declare no conflict of interest

References

1. Holmes, T.R.H.; Crow, W.T.; Yilmaz, M.T.; Jackson, T.J.; Basara, J.B. Enhancing Model-Based Land Surface Temperature Estimates Using Multiplatform Microwave Observations. *Journal of Geophysical Research: Atmospheres* 2013, *118*, 577-591.
2. Wu, P.; Shen, H.; Ai, T.; Liu, Y. Land Surface Temperature Retrieval at High Spatial and Temporal Resolutions Based on Multi-Sensor Fusion. *International Journal of Digital Earth* 2013, *6*, 113-133.
3. Orhan, O.; Ekercin, S.; Dadaser-Celik, F. Use of LANDSAT Land Surface Temperature and Vegetation Indices for Monitoring Drought in the Salt Lake Basin Area, Turkey. *The Scientific World Journal* 2014, *2014*, 1-11.
4. Hulley, G.C.; Hughes, C.G.; Hook, S.J. Quantifying Uncertainties in Land Surface Temperature and Emissivity Retrievals from ASTER and MODIS Thermal Infrared Data. *Journal of Geophysical Research* **2012**, *117*, 1-18.
5. Duan, S.-B.; Li, Z.-L.; Tang, B.-H.; Wu, H.; Tang, R. Generation of a Time-Consistent Land Surface Temperature Product from MODIS Data. *Remote Sensing of Environment* 2014, *140*, 339-349.
6. Weng, Q.; Fu, P. Modeling Annual Parameters of Cleat-Sky Land Surface Temperature Variations and Evaluating the Impact of Cloud Cover Using Time Series of LANDSAT TIR Data. *Remote Sensing of Environment* 2014, *140*, 267-278.
7. Wu, P.; Shen, H.; Zhang, L.; Gottsche, F.-M. Integrated Fusion of Multi-Scale Polar-Orbiting and Geostationary Satellite Observations for the Mapping of High Spatial and Temporal Resolution Land Surface Temperature. *Remote Sensing of Environment* 2015, *156*, 169-181.
8. Weng, Q.; Fu, P.; Gao, F. Generating Daily Land Surface Temperature at LANDSAT Resolution by Fusing LANDSAT and MODIS Data. *Remote Sensing of Environment* 2014, *145*, 55-67.
9. Avdan, U.; Jovanovska, G. Algorithm for Automated Mapping of Land Surface Temperature Using LANDSAT-8 Satellite Data. *Journal of Sensors* 2016, *2016*, 1-8.
10. Bendib, A.; Dridi, H.; Kalla, M.I. Contribution of LANDSAT-8 Data for the Estimation of Land Surface Temperature in Batna City, Eastern Algeria. *Geocarto International* 2016, 10.1080/10106049.2016.1156167, doi:10.1080/10106049.2016.1156167.
11. Mechri, R.; Ottle, C.; Pannekoucke, O.; Kallel, A. Genetic Particle Filter Application to Land Surface Temperature Downscaling. *Journal of Geophysical Research: Atmospheres* 2014, *119*, 2131-2146.
12. Zhou, J.; Dai, F.; Zhang, X.; Zhao, S.; Li, M. Developing a Temporally Land Cover-Based Look-up Table (TL-LUT) Method for Estimating Land Surface Temperature Based on AMSE-E Data Over the Chinese Landmss. *International Journal of Applied Earth Observation and Geoinformation* 2015, *34*, 35-50.
13. Xu, Y.; Shen, Y. Reconstruction of the Land Surface Temperature Time Series Using Harmonic Analysis. *Computers & Geoscience* 2013, *61*, 126-132.

14. Gao, C.; Zhao, E.; Li, C.; Qian, Y.; Ma, L.; Tang, L.; Jiang, X.; Huo, H. Study of Aerosol Influence on Nighttime Land Surface Temperature Retrieval Based on Two Methods. *Advances in Meteorology* **2015**, *2015*, doi:10.1155/2015/496458.
15. Rozenstein, O.; Qin, Z.; Derimian, Y.; Karnieli, A. Derivation of Land Surface Temperature for LANDSAT-8 TIRS Using a Split-Window Algorithm. *Sensors* 2014, *14*, 5768-5780.
16. United States Geological Survey. Using the USGS Landsat 8 Product. Available online: https://landsat.usgs.gov/using-usgs-landsat-8-product (accessed on April 6th).
17. Li, Z.-L.; Tang, B.-H.; Wu, H.; Ren, H.; Yan, G.; Wan, Z.; Trigo, I.F.; Sobrino, J.A. Satellite-Derived Land Surface Temperature: Current Status and Perspective. *Remote Sensing of Environment* **2013**, *131*, 14-37.
18. Li, H.; Liu, Q.; Zhong, B.; Du, Y.; Wang, H.; Wang, Q. A Single-Channel Algorithm for Land Surface Temperature Retrieval from HJ-1B/IRS Data Based on a Parametric Model.
19. Vlassova, L.; Perez-Cabello, F.; Nieto, H.; Martin, P.; Riano, D.; Riva, J.d.l. Assessment of Methods for Land Surface Temperature Retrieval from LANDSAT-5 TM Images Applicable to Multiscale Tree-Grass Ecosystem Modeling. *Remote Sensing* 2014, *6*, 4345-4368.
20. Jimenez-Munoz, J.C.; Sobrino, JA; Gillespie, A.; Sabol, D.; Gustafson, W.T. Improved Land Surface Emissivities Over Agricultural Areas Using ASTER NDVI. *Remote Sensing of Environment* 2006, *103*, 474-487.
21. Weng, Q.; Lu, D.; Schubring, J. Estimation of Land Surface Temperature - Vegetation Abundance Relationship for Urban Heat Island Studies. *Remote Sensing of Environment* 2004, *89*, 467-483.
22. Brunsell, N.A.; Gillies, R. Incorporating Surface Emissivity into a Thermal Atmospheric Correction. *Photogrammetric Engineering and Remote Sensing* 2002, *68*, 1263-1269.
23. Jimenez, M.A.; Mira, A.; Cuxart, J.; Luque, A.; Alonso, S. Verification of a Clear-Sky Mesoscale Simulation Using Satellite-Derived Surface Temperatures. *Monthly Weather Review* 2008, *136*, 5148-5161.
24. Liu, Y.; Hiyama, T.; Yamaguchi, Y. Scaling of Land Surface Temperature Using Satellite Data: A Case Examination on ASTER and MODIS Products over a Heterogeneous Terrain Area. *Remote Sensing of Environment* 2006, *105*, 115-128.
25. Coll, C.; Galve, J.M.; Sanchez, J.M.; Caselles, V. Validation of LANDSAT-7/ETM+ Thermal-Band Calibration and Atmospheric Correction with Ground-Based Measurements. *IEEE Transactions on Geoscience and Remote Sensing* 2010, *48*, 547-555.
26. Guillevic, P.C.; Privette, J.L.; Coudert, B.; Palecki, M.A.; Demarty, J.; Ottle, C.; Augustine, J.A. Land Surface Temperature Product Validation Using NOAA's Surface Climate Observation Networks - Scaling Methodology for the Visible Infrared Imager Radiometer Suite (VIIRS). *Remote Sensing of Environment* 2012, *124*, 282-298.
27. Buriram Municipality. Available online: http://www.buriramcity.go.th/images/datacontent/kong/vichakarn/plan3y2558/section02_2558.pdf (accessed on July 28th).
28. Tourism Authority of Thailand. Buriram. Available online: https://www.tourismthailand.org/About-Thailand/Destination/Buri-Ram (accessed on July 28th).
29. Buriram World. Available online: https://www.buriramworld.com/ (accessed on July 28th).
30. Wang, F.; Qin, Z.; Song, C.; Tu, L.; Karnieli, A.; Zhao, S. An Improved Mono-Window Algorithm for Land Surface Temperature Retrieval from LANDSAT-8 Thermal Infrared Sensor Data. *Remote Sensing* 2015, *7*, 4268-4289.

31. Jimenez-Munoz, J.C.; Sobrino, JA; Skokovic, D.; Matter, C.; Cristobal, J. Land Surface Temperatures Retrieval Methods from LANDSAT-8 Thermal Infrared Sensor Data. *IEEE Geoscience and Remote Sensing Letters* 2014, *11*, 1840-1843.
32. Skokovic, D.; Sobrino, J.A.; Jimenez-Munoz, J.C.; Soria, G.; Julien, Y.; Matter, C.; Cristobal, J. Calibration and Validation of Land Surface Temperature for LANDSAT-8 TIRS Sensor. 2014.
33. Qin, Z.; Karnieli, A.; Berliner, P. A Mono-Window Algorithm for Retrieving Land Surface Temperature from LANDSAT TM Data and Its Application to the Israel-Egypt Border Region. *International Journal of Remote Sensing* 2001, *22*, 3719-3746.
34. Sobrino, JA; Jimenez-Munoz, J.C.; Paolini, L. Land Surface Temperature Retrieval from LANDSAT TM 5. *Remote Sensing of Environment* 2004, *90*, 434-440.
35. Jimenez-Munoz, J.C.; Sobrino, JA A Generalized Single-Channel Method for Retrieving Land Surface Temperature from Remote Sensing Data. *Journal of Geophysical Research* 2003, *108*, 1-9.
36. Liu, L.; Zhang, Y. Urban Heat Island Analysis Using the LANDSAT TM Data and ASTER Data: A Case Study in Hong Kong. *Remote Sensing* 2011, *3*, 1535-1552.
37. Barsi, J.A.; Schott, J.R.; Palluconi, F.D.; Hook, S.J. Validation of a Web-Based Atmospheric Correction Tools for Single Thermal Band Instruments. In Proceedings of Proc. SPIE 5882, Earth Observing Systems X, 58820E, September, 7.
38. Jimenez-Munoz, J.C.; Cristobal, J.; Sobrino, JA; Soria, G.; Ninyerola, M.; Pons, X. Revision of the Single-Channel Algorithm for Land Surface Temperature Retrieval from LANDSAT Thermal-Infrared Data. *IEEE Transactions on Geoscience and Remote Sensing* 2009, *47*, 339-349.
39. Coll, C.; Caselles, V.; Valor, E.; Niclos, R. Comparison between Different Sources of Atmospheric Profiles for Land Surface Temperature Retrieval from Single Channel Thermal Infrared Data. *Remote Sensing of Environment* 2012, *117*, 199-210.
40. Cristobal, J.; Jimenez-Munoz, J.C.; Sobrino, JA; Ninyerola, M.; Pons, X. Improvements in Land Surface Temperature Retrieval from the LANDSAT Series Thermal Band Using Water Vapor and Air Temperature. *Journal of Geophysical Research* 2009, *114*, doi:10.1029/2008JD010616.
41. Chen, F.; Zhao, X.; Ye, H.; Hu, H. Retrieving Land Surface Temperature from LANDSAT TM Using Different Atmospheric Products as Ancillary Data. In Proceedings of Spatial Data Mining and Geographic Knowledge Services (ICSDM), Fuzhou, China.
42. Du, C.; Ren, H.; Qin, Q.; Meng, J.; Zhao, S. A Practical Split-Window Algorithm for Estimating Land Surface Temperature from LANDSAT-8 Data. *Remote Sensing* 2015, *7*, 647-665.
43. Vazquez, D.P.; Reyes, F.J.O.; Arboledas, L.A. A Comparative Study of Algorithms for Estimating Land Surface Temperature from AVHRR Data. *Remote Sensing of Environment* 1997, *62*, 215-222.
44. Yang, J.; Wong, M.S.; Menenti, M.; Nichol, J. Study of the Geometry Effect on Land Surface Temperature Retrieval in Urban Environment. *ISPRS Journal of Photogrammetry and Remote Sensing* 2015, *109*, 77-87.
45. Dash, P. Land Surface Temperature and Emissivity Retrieval from Satellite Measurements. Institut fur Meteorological und Klimaforschung, 2005.
46. Dash, P.; Gottsche, F.M.; Olesen, F.S.; Fischer, H. Land Surface Temperature and Emissivity Estimation from Passive Sensor Data: Theory and Practice-Current Trends. *International Journal of Remote Sensing* 2002, *23*, 2563-2594.
47. Weng, Q. Thermal Infrared Remote Sensing for Urban Climate and Environmental Studies: Methods, Applications, and Trends. *ISPRS Journal of Photogrammetry and Remote Sensing* 2009, *64*, 335-344.

463 48. French, A.N.; Norman, J.M.; Anderson, M.C. A Simple and Fast Atmospheric Correction for Spaceborne
464 Remote Sensing of Surface Temperature. *Remote Sensing of Environment* 2003, *87*, 326-333.
465

466